Downlink Synchronization for OTFS-Based Cellular Systems in High Doppler Environments

MOHAMMED SAQUIB KHAN[1], (Student Member, IEEE), **YEONG JUN KIM**[2],
QASIM SULTAN[1], **JINGON JOUNG**[1], (Senior Member, IEEE),
AND YONG SOO CHO[1], (Senior Member, IEEE)

[1]Department of Electrical and Electronics Engineering, Chung-Ang University, Seoul 06974, South Korea
[2]LG Electronics, Seoul 06772, South Korea

Corresponding author: Yong Soo Cho (yscho@cau.ac.kr)

ABSTRACT This paper proposes a downlink synchronization and cell identity (CID) estimation technique for cellular systems based on orthogonal time-frequency space (OTFS). In the proposed technique, each base station (BS) transmits one detection preamble (DP) and two OTFS symbols (pilot and secondary-CID (SCID) signal (SS)). The DP based on a linear frequency-modulated (LFM) waveform, called proposed-LFM (pLFM), carries the primary-CID (PCID) for symbol timing (ST) synchronization, whereas the SS based on the Zadoff-Chu (ZC) sequence mapped in the delay-Doppler domain carries the SCID. The pLFM is obtained by discretizing the LFM waveform, increasing the frequency sweeping parameter beyond the limit of the operational bandwidth, and incorporating the PCID into the LFM waveform. The autocorrelation and cross-correlation functions of the pLFM are analyzed to examine its correlation properties under the influence of a high Doppler shift. To reduce the undesirable correlation properties (side peak and time ambiguity), a receiver processing (RP) scheme is developed for the pLFM. It is found that the pLFM with RP is suitable for the DP design because it can provide an accurate ST in high-mobility scenarios. In addition, the influence of OTFS modulation on the ZC sequence is derived and a low-complexity detection algorithm based on message passing is applied to detect SCID at the user equipment. The simulation results demonstrate that the proposed downlink synchronization and CID estimation techniques are suitable for OTFS-based cellular systems in high-Doppler environments.

INDEX TERMS Downlink synchronization, Doppler, high-mobility, OTFS, pLFM.

I. INTRODUCTION

Future wireless communication systems are expected to accommodate numerous diverse requirements and usage scenarios, including high-mobility scenarios with a maximum velocity of 500 km/h (high-speed trains) [1], [2]. Currently, the dominant modulation technique of the fourth-generation and fifth-generation New Radio (5G NR) is orthogonal frequency division multiplexing (OFDM), which provides broadband services to a large population [3]. However, OFDM requires accurate frequency synchronization between the transmitter (Tx) and receiver (Rx). In high-mobility scenarios, it may encounter significant intercarrier interference (ICI) and cause carrier frequency offset (CFO).

The associate editor coordinating the review of this manuscript and approving it for publication was Yiming Huo.

Moreover, the CFO is typically caused by the oscillator mismatch between the Tx and Rx or Doppler spread (doubly selective/dispersive) of time-varying channels owing to the swift movement of Tx/Rx [4]. Although conventional transceivers can compensate for the Doppler shift in an ideal environment, the OFDM performance significantly deteriorates owing to the multiple reflections with corresponding CFOs in multipath environments. As the velocity increases, this effect worsens, thus restricting the use of OFDM in high-mobility scenarios.

In order to eliminate or mitigate the impact of ICI, some modifications to conventional OFDM transceivers have been proposed. For instance, linear [5] and non-linear [6] equalizations at Rx, pulse shaping [7] and polynomial cancelation coding [8] at Tx, and a multiple access scheme based on channel-independent block spreading [9] using both Tx and

Rx processing have been proposed. In 5G NR [10], a solution based on variable sub-carrier spacing, called numerology, is adopted to overcome the high Doppler effect in the above-6 GHz bands. Furthermore, Doppler-insensitive or tolerant waveforms/sequences for cell selection [11], random access [12], and positioning [13] for OFDM-based systems have been proposed. Alternatively, some modulation techniques, such as the frequency oversampling technique [14] and vector OFDM [15], have been proposed.

Recently, a novel two-dimensional (2D) modulation technique driven by a delay-Doppler channel, called orthogonal time-frequency space (OTFS), has been proposed [16]. Instead of time-frequency processing as in OFDM, channel representation and information symbol multiplexing in OTFS are performed in the delay-Doppler domain, which is a 2D Fourier dual of the time-frequency channel. The key advantage of delay-Doppler domain processing in OTFS is that it represents the definite geometry of a wireless channel and transforms the well-known time-varying time-frequency channel into a 2D time-invariant delay-Doppler channel. Owing to the advantages of OTFS over OFDM, several studies on channel estimation, detection, and multiple-input multiple-output (MIMO) for OTFS have been proposed. The authors in [16], [17] showed that the packet error rates, peak-to-average power ratio, and MIMO of OTFS are better in high-mobility scenarios than in OFDM-based systems. A multiple access mechanism for an OTFS-based communication system by assigning non-overlapping resource blocks was proposed in [18], making the system multi-user interference free. In [19], a random access preamble (RAP) design technique was proposed to achieve uplink timing synchronization and estimate the timing advance for OTFS-based cellular systems. In [20], a nonorthogonal multiple access (NOMA)-based communication system incorporating OTFS modulation for a heterogeneous mobility scenario was proposed. Here, the users with different mobility patterns are grouped for implementing NOMA, and a suitable performance is achieved in both uplink and downlink by minimizing the intersymbol interference (ISI).

In [21]–[27], estimation techniques for the delay-Doppler channel were investigated because the delay-Doppler channel estimation is necessary at the Rx to perform OTFS demodulation. For single-input single-output OTFS systems, the most straightforward method that can be used to estimate the delay-Doppler channel from the received signal is a threshold method [21] or training pilots, such as pseudo-random noise sequences [22]. In [22], [23], channel estimation was performed in the time-frequency domain, and it was found that this estimation incurs higher implementation complexity than the delay-Doppler channel estimation performed in [24], [25]. For massive MIMO-OTFS systems, the authors in [26] proposed an uplink-aided channel estimation algorithm. In [27], after proving that the 3D channel is sparse, the sparsity was exploited to estimate the channel as a sparse recovery problem. In addition, a two-stage equalization algorithm was proposed in [28], which first equalized the ISI in

the time-domain and then the residual ISI was minimized in the delay-Doppler domain. Thus, OTFS is a promising modulation scheme for next-generation communication systems in high-mobility scenarios.

To use OTFS in a cellular system, initial downlink synchronization and cell searching are necessary. However, it is not easy to perform symbol timing (ST) and cell identity (CID) detection with the received preamble in a high-Doppler environment. A high Doppler shift produces a large ambiguity in the timing estimation and CID detection. The delay-Doppler channel estimation, MIMO, multiple access, detection, and equalization techniques of OTFS described in the abovementioned studies considered an ideal synchronization condition or synchronization with the conventional OFDM-based technique to detect OTFS information symbols. In 5G NR [10], the user equipment (UE) is used to detect the primary synchronization signal (PSS) and secondary synchronization signal (SSS) transmitted from the base station (BS) in a synchronization signal block for ST and CID detection. However, the conventional OFDM-based NR system is sensitive to high Doppler and fails to provide accurate timing synchronization in high-mobility scenarios. By increasing the subcarrier spacing, the Doppler sensitivity can be reduced but at the cost of increased bandwidth (BW). In addition, additional blocks for OFDM-based synchronization and cell searching are required for the initial downlink synchronization and cell searching for OTFS systems. To the best of our knowledge, the ST and CID estimation for OTFS-based cellular systems have not yet been explored.

An energy-based method proposed in [19] for random access with OTFS can be considered for ST and CID estimation. In this method, RAPs are allocated to nonoverlapping contiguous rectangular delay-Doppler resource element (DDRE) groups in the delay-Doppler domain. For each RAP, the energy is transmitted to only one DDRE in its group. Each DDRE group spans the entire delay-domain. If this method is used in the downlink, the required frame size for cell search will be very large because of the requirement of generating a large number of CIDs (1008 in NR [10]) in the cellular systems. Moreover, unlike the UE, the BS transmits signals (synchronization signal, pilot, and user data) continuously to serve multiple UEs in a cell. The UEs at the cell boundary may receive signals from adjacent BSs. Thus, the energy received from the BSs at a UE is normally high, which makes the energy detection approach in downlink synchronization inefficient.

This paper proposes a downlink synchronization and CID estimation technique for OTFS-based cellular systems in a high-Doppler environment. Here, each BS transmits a detection preamble (DP) based on a linear frequency-modulated (LFM) waveform and two OTFS symbols, which comprise two delay-Doppler resource blocks (DDRBs): a pilot DDRB and a secondary-CID (SCID) signal (SS) DDRB based on Zadoff-Chu (ZC) sequence. The DP carries the primary-CID (PCID), which is also used for ST estimation, whereas the SS carries the SCID, like PSS and SSS in NR. By combining

the PCID and SCID obtained from DP and SS, respectively, the UE derives the CID. The DP must be designed such that the ST and PCID are correctly detected in a high-Doppler environment without any prior information (noncoherent detection), such as the PSS in NR. In the proposed technique, the LFM waveform is used for the DP design because the DP should be detected in a high-Doppler environment. The LFM waveforms are widely used for target detection in high-Doppler environments such as RADAR and SONAR systems because the LFM waveform is Doppler-insensitive. However, the location of its correlation peak is shifted depending on the magnitude of the Doppler shift. Thus, the DP designed with the conventional LFM (cLFM) waveform can be successfully detected in a high-Doppler environment but cannot produce the correct timing. In this paper, a proposed-LFM (pLFM)-based DP design technique and receiver processing technique is presented to provide accurate ST estimation and PCID detection in a high-Doppler environment. The autocorrelation and cross-correlation functions of the pLFM-based DP are analyzed to examine its correlation properties under the influence of a high Doppler shift. Subsequently, the effect of OTFS modulation on the ZC sequence is derived for the SS design. In addition, a detection algorithm based on message passing (MP) is introduced to coherently detect SSs at the UE in the presence of multicell interference and noise. Finally, the performance of the proposed downlink synchronization technique is examined with the detection probability in low- and high-mobility cellular environments and compared with the results obtained using the OFDM system.

The remainder of this paper is organized as follows. In Section II, the system model and concept of the proposed downlink synchronization technique for OTFS-based cellular systems are described. In Section III-A, the pLFM-based DP design technique and receiver processing technique are proposed to provide accurate ST estimation and PCID detection in a high-Doppler environment. In Section III-B, the effect of OTFS modulation on the ZC sequence is derived for the SS design. In addition, an MP-based detection algorithm is described to coherently detect SSs at the UE. In Section IV, the performance of the proposed technique is evaluated using a simple model of an OTFS-based cellular system and compared with the conventional OFDM system. The conclusions are presented in Section V.

II. PRELIMINARIES

In an OFDM system, the synchronization signal is mapped in the time-frequency resource grid where the time-domain is partitioned into N symbols and the frequency-domain is partitioned into M subcarriers. The entire time-frequency plane is subdivided into NM resource elements, where each time-frequency resource element (TFRE) is T sec and Δf Hz in width along the time-domain and frequency-domain, respectively, i.e., $\Lambda = \{(nT, m\Delta f), 0 \leqslant n < N, 0 \leqslant m < M\}$. Let $\mathbf{X} \in \mathbb{C}^{N \times M}$ denote a packet of complex symbols mapped on

Λ such that $X[n, m]$ element of $\mathbf{X}$ denotes the nth symbol transmitted on m^{th} subcarrier for $0 \leqslant n < N, 0 \leqslant m < M$. Thus, the complex baseband OFDM signal is given as

$$s(t) = \frac{1}{NM} \sum_{n=0}^{N-1} \sum_{m=0}^{M-1} X[n, m] e^{j2\pi m \Delta f(t - nT)} \quad (1)$$

Practically, (1) is implemented in the discrete time-domain by inverse discrete Fourier transform [29]. Then, $s(t)$ in (1) passes over a wireless multipath channel comprising P discrete propagation paths. In most cases where the UE and/or scatters are immobile or have low velocity, the OFDM system is considered linear time-invariant (LTI). When the transmitted signal is received by passing through multiple scatters, it is temporally smeared out. However, if the channel impulse response (CIR) is time-invariant, a one-dimensional delay-domain CIR, $h(\tau)$, is sufficient to characterize the time-dispersive channel (or frequency-selective channel).

In systems where the UE is highly mobile and operates at a higher carrier frequency (such as millimeter-wave), the assumption of LTI CIRs may no longer be valid. Thus, several previous studies have adopted a linear time-variant (LTV) channel model [30] for high-mobility scenarios. Because of the presence of the Doppler effect in high-mobility scenarios, the LTV channels induce a frequency shift, which causes the signal spectrum to be smeared (i.e., frequency-dispersive). In fact, as the Doppler effect and dispersive multipath propagation coexist in the LTV channels, they are usually doubly selective. Therefore, in a high-mobility environment, the received signal at the UE can be expressed as

$$r(t) = \int_{-\infty}^{\infty} h(t, \tau) s(t - \tau) d\tau + w(t), \quad (2)$$

where $h(t, \tau)$ is the LTV time-delay CIR:

$$h(t, \tau) = \sum_{i=1}^{P} \beta_i e^{-j2\pi v_i t} \delta(\tau - \tau_i(t)), \quad (3)$$

P, β_i, v_i, τ_i, $\delta(\cdot)$, and $w(t)$ denote the number of resolvable paths, complex gain, Doppler (relative to the carrier frequency), delay of ith path, impulse function, and additive white Gaussian noise (AWGN), respectively. In an OFDM based system, the LTV channel can be represented in the time-delay domain, $h(t, \tau)$, or equivalently time-frequency domain, $H(t, f)$ [30]. The time-frequency channel, $H(t, f)$, can be obtained by taking the Fourier transform (FT) of the time-delay domain channel, $h(t, \tau)$, along τ as follows:

$$H(t, f) = \int_{-\infty}^{\infty} h(t, \tau) e^{-j2\pi f \tau} d\tau \quad (4)$$

Although the time-delay and time-frequency domain representations of LTV channels have been extensively used under high-mobility scenarios, they have limited support and are characterized by a maximum delay spread ($\propto$ 1/coherence

time) and maximum Doppler spread ($\propto$ 1/coherence BW). Owing to the high mobility, the channel in the time-delay or time-frequency domain changes rapidly, which makes channel estimation difficult and incurs huge overhead. Therefore, LTV channels are physically meaningful and intuitively characterized in terms of time delays and Doppler shifts. By expressing the FT of the time-delay channel, $h(t, \tau)$, along t, the delay-Doppler channel can be obtained as

$$h(\tau, v) = \int_{-\infty}^{\infty} h(t, \tau) e^{-j2\pi vt} dt \qquad (5)$$

The delay-Doppler domain representation of the channel captures the actual geometry of the channel by characterizing the reflectivity of scatterers associated with all paths having an independent delay value (with respect to the scatterer's relative distance) and Doppler value (with respect to the scatterer's relative velocity).

Motivated by the properties of the delay-Doppler domain channel representation in high-mobility scenarios, the authors in [16] developed the OTFS modulation scheme. OTFS modulation efficiently transforms the time-varying fading channel into a time-independent nonfading channel, as follows:

$$h(\tau, v) = \int_{-\infty}^{\infty} \int_{-\infty}^{\infty} H(t, f) e^{-j2\pi(vt - f\tau)} dt df \qquad (6)$$

In OTFS, the symbols are mapped on a discretized $N \times M$ resource block in the delay-Doppler domain, called DDRB. The symbols are T sec and Δf Hz in width along the Doppler-domain and delay-domain, respectively. Each DDRE in the DDRB is $1/NT$ Hz and $1/M\Delta f$ sec in width along the Doppler-domain and delay-domain, respectively, i.e., $\Gamma = \left\{ \left(\frac{k}{NT}, \frac{l}{M\Delta f} \right), 0 \leqslant k < N, 0 \leqslant l < M \right\}$. The information symbols in the delay-Doppler domain, $x[k, l]$, are then transformed in the familiar time-frequency domain, $X[n, m]$, using a transform called the 2D inverse symplectic finite FT (ISFFT):

$$X[n, m] = \frac{1}{MN} \sum_{k=0}^{N-1} \sum_{l=0}^{M-1} x[k, l] e^{-j2\pi \left(\frac{ml}{M} - \frac{nk}{N} \right)} \qquad (7)$$

Thus, the OTFS resultant waveform in time-domain is the fluctuating pulse train, shifted in time equal to the delay, $l_p/M\Delta f$, and in frequency equal to Doppler k_p/NT, where p is the index of DDRE. In other words, the time-domain waveform of OTFS inherits the combinational and beneficial properties of well-known multiple access techniques. The time-domain OTFS waveform is locally localized in the time-domain like time-division multiple access, globally localized in the Doppler-domain like OFDM, and spreads like code-division multiple access in the delay-Doppler domain.

Let us consider a cellular system in which a UE performs cell search by receiving the downlink frame transmitted from multiple BSs located at their predefined locations, as shown in Fig. 1. With the downlink signals received from adjacent
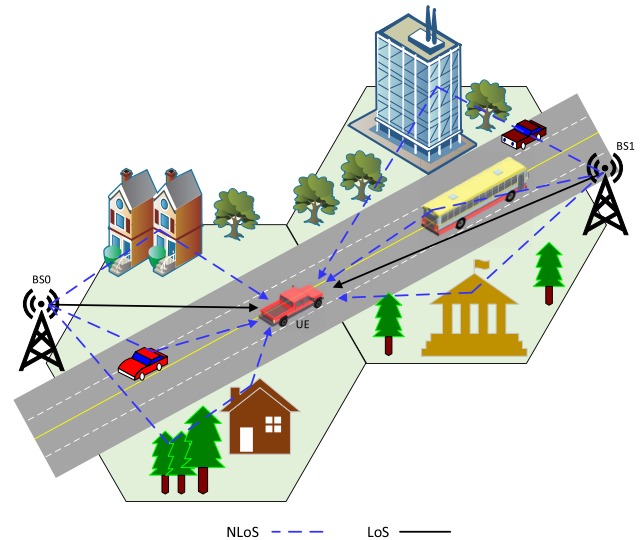

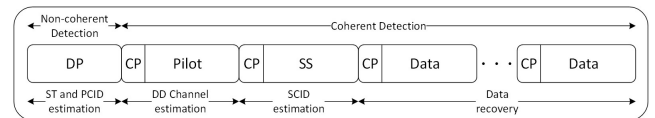**FIGURE 1. Example of a cellular system with two BSs.**

FIGURE 2. Downlink frame structure.

BSs, the UE needs to perform synchronization and CID estimation to detect the serving cell. An accurate ST estimation is also required for the channel estimation. In the proposed technique, each BS transmits a downlink synchronization frame comprising a DP, a pilot, and an SS, as shown in Fig. 2. The DP should be found at the Rx by using a noncoherent detection scheme because the channel state information and timing information are not available at the start of synchronization. The DP is used to determine the ST and PCID at the Rx by maximizing the cross-correlation between the transmitted and received signals. Using the ST information, a pilot is detected in the delay-Doppler domain. Using the channel information obtained by the pilot, the SS (SCID) is detected coherently in the delay-Doppler domain. The CID of the BS is then obtained by combining the PCID and SCID.

The selection of synchronization signals is crucial because they are the first signals that the UE needs to identify without any prior information before accessing the network. In LTE, the ZC sequence is used as the PSS and is always mapped to 72 subcarriers at the center of the carrier BW. In 5G NR, the m-sequence is used as a PSS and can be mapped to 127 active subcarriers at multiple locations on the entire carrier BW [10]. These sequences possess good autocorrelation properties for accurate ST estimation [31]. However, they may be unsuitable for synchronization in high-mobility environments because of their sensitivity to the high Doppler effect. For the ZC sequence, the influence of Doppler shift is studied and the solutions are provided in [31], [32]. However,

the solutions in [31], [32] are not applicable to high-frequency bands, and correspondingly, higher Doppler shifts. Hence, these sequences may cause high ambiguity in ST estimation in a high-Doppler environment and degrade the performance of the initial synchronization. Therefore, this paper proposes a pLFM waveform to provide accurate ST estimation and PCID detection in a high-Doppler environment. After completing the ST synchronization with the DP, the pilot transmitted in the delay-Doppler domain (OTFS modulation) is used to estimate the delay-Doppler channel. Finally, the SS in the delay-Doppler domain is used to detect the SCID with the delay-Doppler channel estimated by the pilot. Because the ZC sequence possesses good correlation properties and can be used to generate a large number of SCIDs, it is selected as an SS where the SCID is mapped to its root index.

When the signal transmitted from the cth BS is $s^c(t)$ and the number of adjacent BSs is C, the signal received at the UE in the time-domain is given by

$$r(t) = \sum_{c=0}^{C-1} \int \int h^c(\tau, v) s^c(t - \tau) e^{j2\pi v(t-\tau)} d\tau dv + w(t)$$

(8)

Here, the delay-Doppler channel is defined as [22], [33], [34]:

$$h^c(\tau, v) = \sum_{i=1}^{P} \beta_i^c \delta\left(\tau - \tau_i^c\right) \delta\left(v - v_i^c\right)$$

(9)

where $0 \leqslant \tau_i^c \leqslant \tau_{\max}$ and $-v_{\max} \leqslant v_i^c \leqslant v_{\max}$. Here, $v_{\max}$ and $\tau_{\max}$ are the maximum Doppler and delay spreads, respectively. The delay and Doppler shift taps for the ith path are $\tau_i^c = l_i^c / M \Delta f$ and $v_i^c = \left(k_i^c + \kappa_i^c\right) / NT$, respectively. Here, $0 \leqslant l_i^c \leqslant l_{\max}$, $-k_{\max} \leqslant k_i^c \leqslant k_{\max}$, $l_{\max}$, and $k_{\max}$ denote the delay index of the ith path, Doppler index of the ith path, largest index of delay tap, and largest index of Doppler tap, respectively. In addition, $\kappa_i^c \in [-0.5, 0.5]$ denotes the fractional Doppler frequency associated with the ith path.

III. PROPOSED DOWNLINK SYNCHRONIZATION TECHNIQUE FOR OTFS

A. DETECTION PREAMBLE (DP) DESIGN

To analyze and characterize the properties and behavior of the waveforms paired with the matched filter, the ambiguity function (AF) is extensively used, which can be expressed as

$$\chi(\tau, v) = \int_{-\infty}^{\infty} s(t - \tau) s^*(t) e^{j2\pi vt} dt$$

(10)

The AF is useful for examining the resolution, side-lobe behavior, and ambiguities in both Doppler and delay (time shift) domains of a given waveform. Fig. 3 shows the time-domain waveforms (pulse in Fig. 3a and cLFM in Fig. 3b); their corresponding AF contours are presented in Fig. 3d. When the Doppler shift is zero, the AF of the pulse
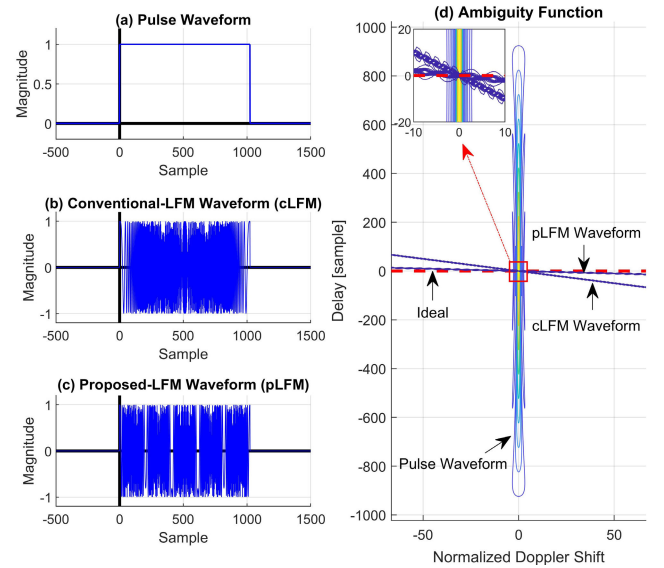
FIGURE 3. (a) Pulse, (b) conventional-LFM (cLFM), (c) proposed-LFM (pLFM), and (d) ambiguity functions of pulse, cLFM ($b = B = 15.36$ MHz), and pLFM (receiver processing, $\alpha = 5$ and $N_{pLFM} = 1024$).

waveform with a duration of T follows a triangular function along the delay axis (Fig. 3d). At zero delay, the AF of the pulse waveform follows a *sinc* function along the Doppler axis and becomes zero at a Doppler mismatch of $\pm 1/\tau$ Hz. Therefore, the peak of the pulse waveform's AF remains at the correct timing when the Doppler mismatch is small $\left(< 1/\tau\right)$. However, in the case of a nonnegligible Doppler shift, the pulse waveform cannot be detected.

The cLFM waveform is extensively used for surveillance and tracking applications in which the target must be detected in a high-mobility environment. A time-domain cLFM waveform with a frequency sweeping parameter b and symbol duration T is given as [35]

$$x_{LFM}(t) = e^{j\pi \frac{b}{T} t^2}, \quad 0 \leqslant t < T, 0 < b \leqslant B$$

(11)

where B denotes the operational BW. Unlike the pulse waveform, the parameters of the cLFM waveform (b and T) can be used independently to regulate the delay resolution and pulse energy. The AF of the cLFM waveform is a triangular ridge skewed in the delay-Doppler plane (Fig. 3d). It can provide significant peaks at the output of the matched filter for a broad range of Doppler shifts, which follow a *sinc* function along the Doppler axis at zero delay. However, its peak is shifted in time proportional to the Doppler shift. The timing accuracy obtained by the cLFM waveform is constrained by b and T; it improves as b increases and/or T decreases. Generally, the value of b in cLFM is set to B because it is known to exhibit the best performance of the LFM waveform. The AF of the cLFM waveform (skewed triangular ridge) is beneficial for surveillance applications (only for detection). However, for ST estimation, AF of a waveform that provides high peaks at the correct timing regardless of any Doppler shift value is beneficial. Thus, an ideal AF for an accurate ST

estimation in high-Doppler environments would be "a line" centered on the horizontal (Doppler shift) axis, as shown in Fig. 3d. This subsection (III-A) aims to identify a waveform that has an AF (pLFM in Fig. 3d) close to the ideal AF, so that the DP is detected with accurate ST in high-Doppler environments.

The pLFM is obtained by discretizing the cLFM waveform, increasing the frequency sweeping parameter beyond the limit of B and incorporating PCID in the cLFM waveform. By selecting the frequency sweeping parameter value as an integer multiple of B, the pLFM can be defined as

$$x_{pLFM}^{u_1}\left(n_{pLFM}\right) = e^{j\pi \frac{u_1 \omega n_{pLFM}^2}{N_{pLFM}}} \tag{12}$$

where $u_1 \in \{1, -1\}$ is the PCID, and $\omega = \alpha b T_s$, and $\alpha \in \mathbb{N}$. Here, $t = n_{pLFM} T_s$ and $T_s = T / N_{pLFM}$. T_s and N_{pLFM} denote the sampling time and number of samples in T, respectively. As ω exceeds one, the signal in (12) becomes a repetitive pattern because the pLFM is discretized in the time-domain. For instance, when $\omega = 5$ in (12), the cLFM waveform with $b = B$ and symbol duration $T/5$ repeats five times over a given duration T, as shown in Fig. 3c. The DP is constructed using a pLFM signal at the BS.

At the Rx (UE), the ST and PCID are obtained noncoherently by correlating the received signal with the locally generated reference DPs. The correlation between the received signal with v and the reference DP is given by

$$R_{pLFM}^{u_1 u_1'}\left(m_{pLFM}, v\right)$$
$$\triangleq \sum_{n_{pLFM}=-\infty}^{\infty} x_{pLFM}^{u_1}\left(n_{pLFM}\right) \left[x_{pLFM}^{u_1'}\left(n_{pLFM} - m_{pLFM}\right)\right]^* e^{\frac{j2\pi v T n_{pLFM}}{N_{pLFM}}}$$
$$= e^{-j\pi \frac{\omega u_1' m_{pLFM}^2}{N_{pLFM}}}$$
$$\sum_{n_{pLFM}=-\infty}^{\infty} e^{j\pi \frac{n_{pLFM}}{N_{pLFM}}\left(\omega u_1 n_{pLFM} - \omega u_1' n_{pLFM} + 2\omega u_1' m_{pLFM} + 2vT\right)} \tag{13}$$

where $*$ denotes the complex conjugate. If $u_1 = u_1'$, the autocorrelation function of pLFM can be derived as

$$R_{pLFM}^{u_1 u_1}\left(m_{pLFM}, v\right)$$
$$\triangleq e^{-j\pi \frac{u_1 \omega m_{pLFM}^2}{N_{pLFM}}} \sum_{n_{pLFM}=0}^{N_{pLFM}-1} e^{\frac{j2\pi n_{pLFM}}{N_{pLFM}}\left(u_1 \omega m_{pLFM} + vT\right)}$$
$$\triangleq e^{j\pi vT\left(1 + m_{pLFM}/N_{pLFM}\right)} e^{j\pi u_1 \omega m_{pLFM}}$$
$$\begin{cases} \dfrac{\sin\left(\frac{\pi\left(u_1 \omega m_{pLFM} + vT\right)\left(N_{pLFM} - m_{pLFM}\right)}{N_{pLFM}}\right)}{\sin\left(\frac{\pi\left(u_1 \omega m_{pLFM} + vT\right)}{N_{pLFM}}\right)}, & m_{pLFM} \geqslant 0 \\[4mm] \dfrac{\sin\left(\frac{\pi\left(u_1 \omega m_{pLFM} + vT\right)\left(N_{pLFM} + m_{pLFM}\right)}{N_{pLFM}}\right)}{\sin\left(\frac{\pi\left(u_1 \omega m_{pLFM} + vT\right)}{N_{pLFM}}\right)}, & m_{pLFM} < 0 \end{cases}$$
$$\tag{14}$$

where $-N_{pLFM} < m_{pLFM} < N_{pLFM}$. Note that the correlation operation is performed over the full period of pLFM (N_{pLFM}). In (14), when $m_{pLFM} = 0$ and $v = 0$, $\left|R_{pLFM}^{u_1 u_1}(0, 0)\right| = N_{pLFM}$. If $u_1 \neq u_1'$, $u_1 = 1$, cross-correlation function can be derived as follows:

$$R_{pLFM}^{u_1 u_1'}\left(m_{pLFM}, v\right)$$
$$\triangleq e^{j\pi \frac{\omega m_{pLFM}^2}{N_{pLFM}}} \sum_{n_{pLFM}=-\infty}^{\infty} e^{\frac{j2\pi n_{pLFM}}{N_{pLFM}}\left(\omega\left(n_{pLFM} - m_{pLFM}\right) + vT\right)}$$
$$= e^{j\pi \frac{\omega m_{pLFM}^2}{N_{pLFM}}} \frac{e^{-j\pi \frac{\left(vT - \omega m_{pLFM}\right)^2}{2\omega N_{pLFM}}}}{\sqrt{-j2\omega/N_{pLFM}}}$$
$$\sum_{n_{pLFM}=-\infty}^{\infty} e^{-j\pi \frac{N_{pLFM} n_{pLFM}^2}{2\omega}} e^{j2\pi \frac{n_{pLFM}\left(vT - \omega m_{pLFM}\right)}{2\omega}}$$
$$= \frac{e^{\frac{j\pi}{N_{pLFM}}\left(\omega m_{pLFM}^2 - \frac{\left(vT - \omega m_{pLFM}\right)^2}{2\omega}\right)}}{\sqrt{-j2\omega/N_{pLFM}}}$$
$$\vartheta_3\left(\frac{\pi\left(vT - \omega m_{pLFM}\right)}{2\omega}, e^{-j\pi \frac{N_{pLFM}}{2\omega}}\right)$$
$$\tag{15}$$

where $\vartheta_3\left(z_1, z_2\right) \equiv \sum_{n_{pLFM}=-\infty}^{\infty} z_2^{n_{pLFM}^2} e^{j2z_1 n_{pLFM}}$ is the Jacobi theta-3 function with $z_1 = \pi\left(vT - \omega m_{pLFM}\right)/2\omega$ and $z_2 \equiv e^{j\pi\left(-N_{pLFM}/2\omega\right)}$ [36].

Fig. 4 shows the autocorrelation and cross-correlation functions of the pLFM waveform when $N_{pLFM} = 1024$, $T = 66.67\mu s$, $b = B = 15.36$ MHz, and $v = 0$. In this figure, $\omega = 1$ corresponds to the case of cLFM. As ω increases, the autocorrelation function (Fig. 4a) in the region of origin ($m_{pLFM} = 0$) becomes sharper (although only slightly), which implies a slight increase in the timing estimation accuracy. Fig. 4b shows that increasing ω does not degrade the cross-correlation function property. The mean value of cross-correlation function (for $\omega \in [1, 10]$) is $0.066 \approx 2/\sqrt{N_{pLFM}}$. Moreover, the analytical results for both autocorrelation function in (14) and cross-correlation function in (15) agree well with the simulation results presented in Figs. 4a and 4b, respectively.

As ω increases, the time–BW product of pLFM increases, which in turn decreases its Doppler sensitivity. However, an increase in ω also increases the side peaks in the autocorrelation function (Fig. 4a), which may produce time ambiguity. To reduce the effect of side peaks and obtain a higher time–BW product, a receiver processing (RP) scheme is developed for pLFM, as shown in Fig. 5. Here, the received DP of N_{pLFM} samples is segmented into α fragments each of $N_{pLFM}^{\alpha} = \left\lfloor N_{pLFM}/\alpha \right\rfloor$ samples. Then, each fragment is correlated with a locally generated DP with ω (N_{pLFM}^{α} samples) to reduce the Doppler effect by α. When the RP
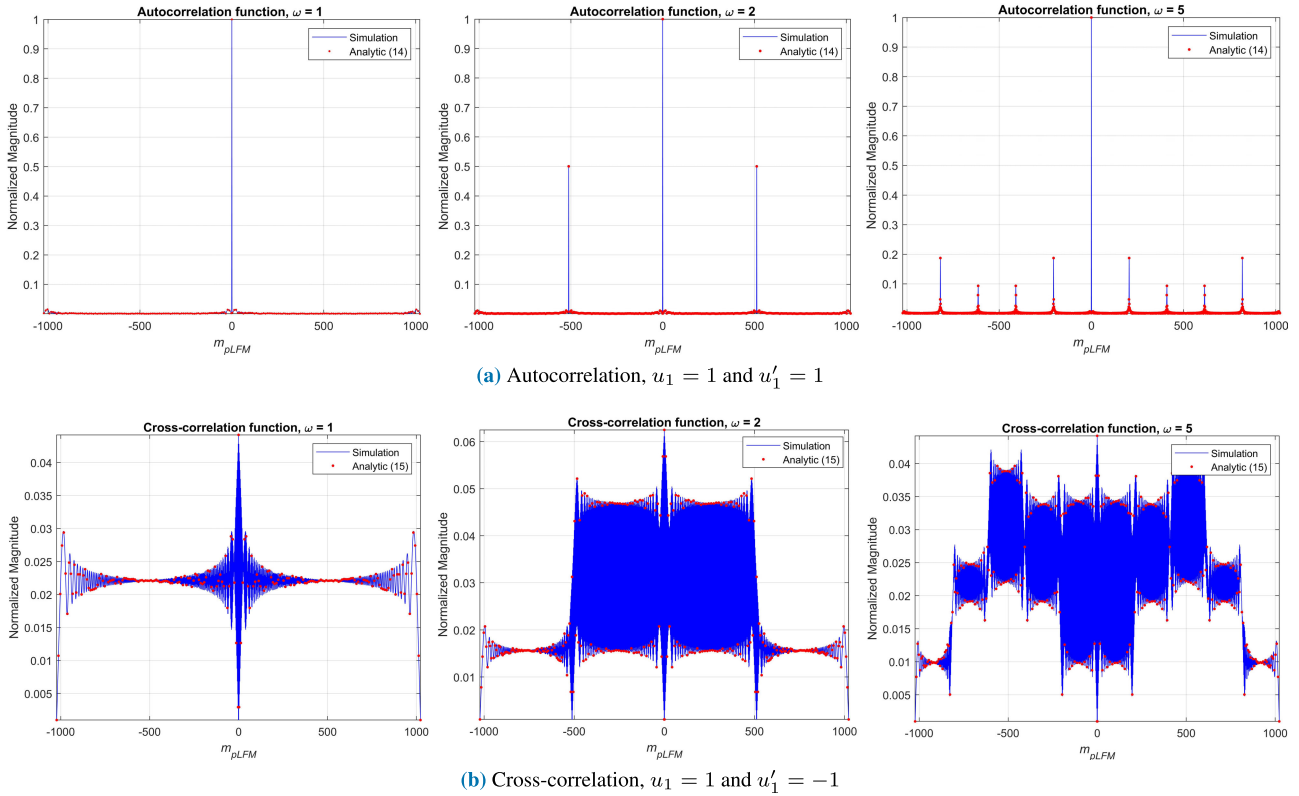
(a) Autocorrelation, $u_1 = 1$ and $u_1' = 1$

(b) Cross-correlation, $u_1 = 1$ and $u_1' = -1$

FIGURE 4. Comparison of simulation and analytic results of correlation property of pLFM with $v = 0$.

scheme is applied to pLFM, (14) becomes

$$
R_{pLFM,\mathrm{RP}}^{u_1 u_1}\left(m_{pLFM}^{\alpha}, v\right)
$$

$$
= e^{j\pi \frac{v}{\alpha} T\left(1 + m_{pLFM}^{\alpha} / N_{pLFM}^{\alpha}\right)} e^{j\pi u_1 \frac{\omega}{\alpha} m_{pLFM}^{\alpha}}
$$

$$
\begin{cases}
\dfrac{\sin\left(\dfrac{\pi\left(u_1 \omega m_{pLFM}^{\alpha} + vT\right)\left(N_{pLFM}^{\alpha} - m_{pLFM}^{\alpha}\right)}{\alpha N_{pLFM}^{\alpha}}\right)}{\sin\left(\dfrac{\pi\left(u_1 \omega m_{pLFM}^{\alpha} + vT\right)}{\alpha N_{pLFM}^{\alpha}}\right)}, & m_{pLFM}^{\alpha} \geqslant 0 \\[4ex]
\dfrac{\sin\left(\dfrac{\pi\left(u_1 \omega m_{pLFM}^{\alpha} + vT\right)\left(N_{pLFM}^{\alpha} + m_{pLFM}^{\alpha}\right)}{\alpha N_{pLFM}^{\alpha}}\right)}{\sin\left(\dfrac{\pi\left(u_1 \omega m_{pLFM}^{\alpha} + vT\right)}{\alpha N_{pLFM}^{\alpha}}\right)}, & m_{pLFM}^{\alpha} < 0
\end{cases}
$$

$$(16)$$

where $-N_{pLFM}^{\alpha} < m_{pLFM}^{\alpha} < N_{pLFM}^{\alpha}$. In (16), when $m_{pLFM}^{\alpha} = 0$ and $v = 0$, the correlation output of each correlator gives a peak value of $\left| R_{pLFM,\mathrm{RP}}^{u_1 u_1}(0, 0) \right| = N_{pLFM}^{\alpha}$. Using only one correlator, the performance of pLFM is restricted to N_{pLFM}^{α}, which is α times less than that of cLFM (when no Doppler effect exists). Because pLFM is robust to the Doppler effect, each correlator's output is coherently combined to achieve a performance gain equal to N_{pLFM} (same as the performance of cLFM in the absence of Doppler effect). This process is repeated for each value of u_1 and the PCID is estimated.

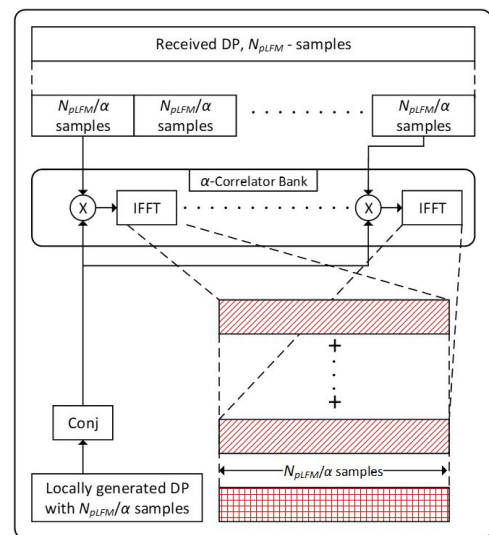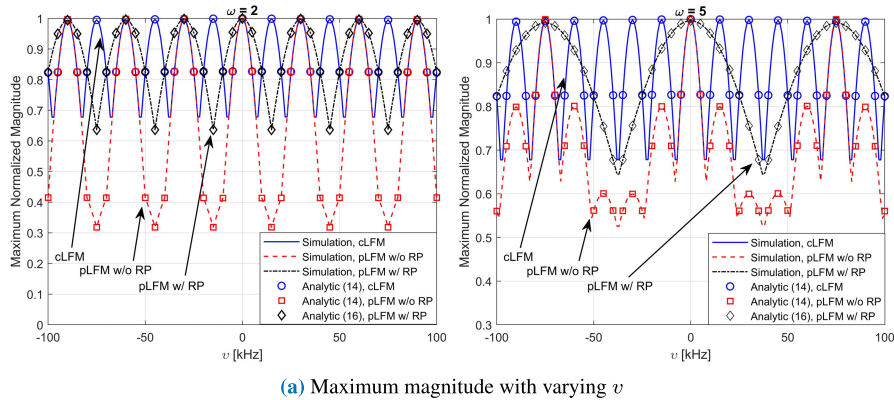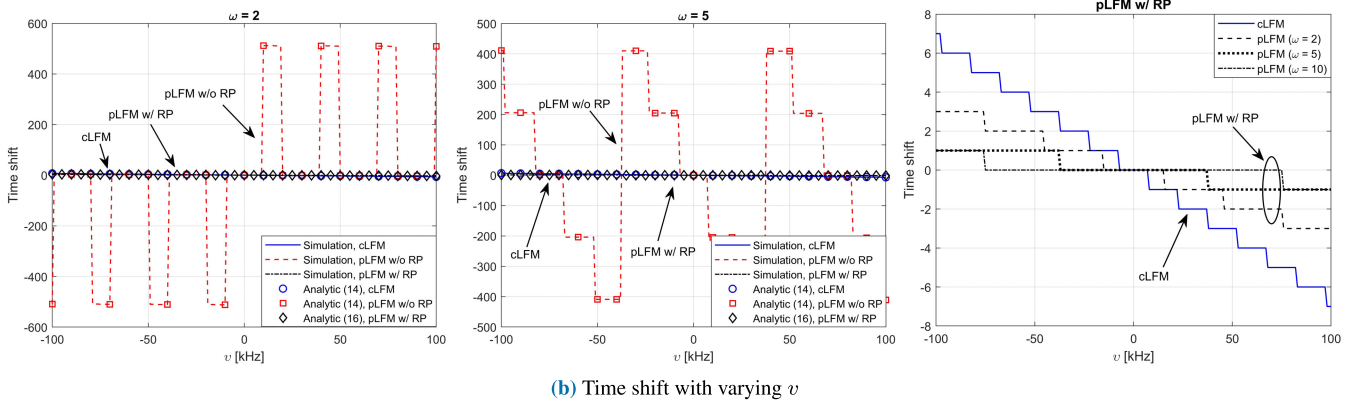When $v \neq 0$, (16) can be viewed as a time-shifted version of a *sinc* function. With the proposed RP,

FIGURE 5. Receiver processing for STS and PCID detection.

the time shift, $\tilde{m}_{pLFM}^{\alpha}$, corresponding to the maximum value $\left| R_{pLFM,\mathrm{RP}}^{u_1 u_1}(0, v) \right|$ can be expressed as

$$
\tilde{m}_{pLFM}^{\alpha} = -\frac{u_1 \omega T v}{\alpha^2},
$$

$$
R_{pLFM,\mathrm{RP}}^{u_1 u_1}(0, v) = \left| \mathrm{sinc}\left(\tilde{m}_{pLFM}^{\alpha}\right) \right|
$$

$$(17)$$

(a) Maximum magnitude with varying v

(b) Time shift with varying v

FIGURE 6. Comparative simulation and analytic results of pLFM with varying *v*.

Eq. (17) indicates that when B and T are fixed, the time shift increases and decreases proportionally with v and α, respectively. Moreover, $\left| R^{u_1 u_1}_{pLFM,\mathrm{RP}}(0, v) \right|$ decreases as $\tilde{m}^\alpha_{pLFM}$ increases. The ST estimation should be sufficiently accurate because it is used to detect the start of OTFS symbols. Otherwise, the symbol timing offset (i.e., time shift) will produce a cyclic shift in delay-domain, thereby introducing interference in the received OTFS symbols in the delay-Doppler domain.

Fig. 6 illustrates the comparative simulation and analytic results of cLFM and pLFM (with and without RP) in the existence of a Doppler shift; that is, $v \neq 0$. In the simulation, for a fair comparison, the same values of B and T are used in both cLFM and pLFM. Figs. 6a and 6b show the maximum magnitude and time shift in the autocorrelation function of pLFM, respectively, with varying v, $N_{pLFM} = 1024$, $T = 66.67\mu s$, $b = B = 15.36$ MHz, and $\omega \in \{1, 2, 5\}$. Fig. 6a and the first two figures in Fig. 6b indicate that the analytical results in (14) and (16) agree well with the simulation results. The third figure in Fig. 6b indicates a detailed version of the time shift of cLFM and pLFM with RP. These figures indicate that when $v = 0$, the maximum magnitude is one for both cLFM and pLFM (for any value of ω) and no time shift occurs. However, the maximum magnitude fluctuates following a *sinc* function proportional to the Doppler shift, and a corresponding time shift occurs. For cLFM (i.e., $\omega = 1$), when $v = \pm 8$ kHz, the maximum magnitude is 0.68 and the time shift is one

sample. Similarly, for the pLFM without RP (with the same $v = \pm 8$ kHz), when $\omega \in \{2, 5\}$, the maximum magnitude is $\{0.41, 0.63\}$ and the time shift is $\{512, 205\}$ samples. However, for the pLFM with RP, the maximum magnitude is $\{0.68, 0.65, 0.64\}$ and the time shift of one sample occurs at $v \in \pm\{16, 38, 76\}$ kHz when $\omega \in \{2, 5, 10\}$. That is, for the pLFM with RP, the time shift does not occur until v reaches $\{16, 38, 76\}$ Hz when $\omega \in \{2, 5, 10\}$. For cLFM, a time shift occurs when $v = \pm 8$ kHz. Thus, the time shift decreases as ω in pLFM with RP increases. Because an accurate ST estimation in a high-Doppler environment is crucial in downlink synchronization, pLFM with RP is used for DP design.

When the C BSs transmit their DPs, the signal received at the UE can be expressed as

$$r_{pLFM}(t) = \beta^{c'}_i s^{c'}_{pLFM} \left(t - \tau^{c'}_i \right) e^{j2\pi v^{c'}_i \left(t - \tau^{c'}_i \right)} + \tilde{w}(t)$$

$$\tilde{w}(t) = \sum_{c=0, c \neq c'}^{C-1} \sum_{i=1}^{P} \beta^c_i s^c_{pLFM} \left(t - \tau^c_i \right) e^{j2\pi v^c_i \left(t - \tau^c_i \right)} + w(t)$$

$$(18)$$

where $s^{c'}_{pLFM}(t) = x^{u'_1}_{pLFM}(t)$ denotes the pLFM signal transmitted from the desired BS c' and $\tilde{w}(t)$ denotes the interference signals from other BSs and noise. ST and PCID are acquired at the UE when the DP is detected at the output of
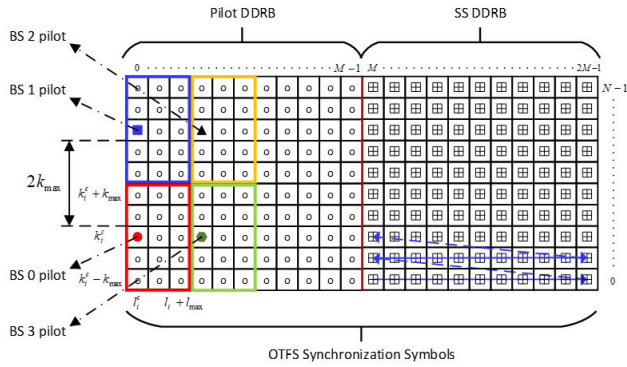
FIGURE 7. Frame structure of OTFS for synchronization (o: zeros and ⊞: elements of ZC sequence).

the pLFM correlator, as follows:

$$\left[u_1', \tilde{\tau}^{c'}\right] = \arg\max_{c, t \in [0, T_W]} \left|\tilde{R}_{pLFM}^c(t)\right|^2 > \gamma \qquad (19)$$

where $\tilde{\tau}^{c'}$, T_W, and γ denote the estimated ST of the desired BS c', the length of the correlator window, and a predefined threshold value, respectively. The output of the pLFM correlator for the cth BS can be expressed as follows:

$$\tilde{R}_{pLFM}^c(t) = \int_0^{T_W} r_{pLFM}(t + \tau) \left[s_{pLFM}^c(\tau)\right]^* d\tau \qquad (20)$$

B. SECONDARY-CID SIGNAL (SS) DESIGN

After transmitting the DP, each BS transmits two OTFS symbols comprising two OTFS DDRBs, as shown in Fig. 7. In the first DDRB, a pilot signal is mapped at one DDRE in Γ as:

$$x_p^c[k, l] = \begin{cases} 1 & \text{if } k = k_p^c, l = l_p^c \\ 0 & \text{Otherwise} \end{cases} \qquad (21)$$

where $\left(k_p^c, l_p^c\right)$ is a DDRE allocated to the cth BS. For the UE located at the cell edge, the delay of certain paths from the serving BS to the UE can be as high as τ_{max}. Thus, the signal received through these paths at the UE may possess an offset in the delay-Doppler domain and cause intercell interference unless the pilot of each BS does not overlap in the DDRB. To ensure that the pilot can be received at the UE without interference, each BS's pilot has some DDREs reserved around it such that $k_i^{c+1} - k_i^c > 2k_{max}$, $l_i^{c+1} - l_i^c > l_{max}$. Following the pilot, the SS generated using a ZC sequence with root index u_2 and sequence length MN is mapped in the next DDRB, such that

$$x_{SS}^{u_2}[k, l] = e^{-\frac{j\pi u_2}{MN}(l + kM)(l + kM + 1)}, \quad 0 \leqslant k < N, \ 0 \leqslant l < M \qquad (22)$$

The SCID is mapped to the root index u_2 of the ZC sequence.

The relation between delay-Doppler ZC and time-frequency ZC is given as

$$X_{SS}^{u_2}[n, m] = \frac{1}{MN} \sum_{k=0}^{N-1} \sum_{l=0}^{M-1} x_{SS}^{u_2}[k, l] e^{j2\pi \left(\frac{nk}{N} - \frac{ml}{M}\right)}$$

$$= \frac{1}{M} \sum_{l=0}^{M-1} \left(e^{-\frac{j2\pi}{MN}(mN+n)l} e^{-\frac{j\pi u_2}{MN}(-\hat{u}_2^2 n^2 + \hat{u}_2 n)}\right.$$

$$\left. \frac{1}{N} \sum_{k=0}^{N-1} x_{SS}^{u_2}[k - \hat{u}_2 n/M, l]\right)$$

$$= e^{\frac{j\pi u_2}{MN}(\hat{u}_2 n(\hat{u}_2 n - 1))} \frac{1}{M} \sum_{l=0}^{M-1} \hat{X}_{SS}^{u_2}[0, l] e^{-\frac{j2\pi}{M}\left(\frac{mN+n}{N}\right)l}$$

$$= x_{SS}^{u_2*}[0, \hat{u}_2 n] \hat{x}_{SS}^{u_2}\left[\frac{mN+n}{N}, 0\right] \qquad (23)$$

Here $\hat{u}_2$ is the multiplicative inverse of u_2 such that $u_2\hat{u}_2 \bmod MN = 1$. Hence, the ISFFT of a ZC sequence becomes another ZC sequence. Now, the time-frequency ZC, $X_{SS}^{u_2}[n, m]$ in (23), is converted to time-domain to show the relation between delay-Doppler ZC and time-domain ZC as

$$s_{SS}^{u_2}(t)$$

$$= \begin{cases} \sum_{m=0}^{M-1} \sum_{n=0}^{N-1} X_{SS}^{u_2}[n, m] e^{j2\pi m \Delta f(t - nT)} & 0 \leqslant t < NT \\ 0 & \text{Otherwise} \end{cases}$$

$$= \sum_{m=0}^{M-1} \left(e^{-\frac{j\pi u_2}{MN}(m^2 M^2 N^2 + mMN - 2\hat{u}_2 mMN \Delta ft)}\right.$$

$$\left. \sum_{n=0}^{N-1} x_{SS}^{u_2*}[0, \hat{u}_2 n - u_2 mMN] \hat{x}_{SS}^{u_2}\left[\frac{mN+n}{N}, 0\right]\right)$$

$$= \sum_{m=0}^{M-1} \left(e^{-\frac{j\pi u_2}{MN}\left[(mMN - \hat{u}_2 \Delta ft)(mMN - \hat{u}_2 \Delta ft + 1) - (\hat{u}_2^2 \Delta f^2 t^2 - \hat{u}_2 \Delta ft)\right]}\right.$$

$$\left. \sum_{n=0}^{N-1} X_{SS}^{u_2}[\hat{u}_2 n - u_2 mMN, m]\right)$$

$$= e^{\frac{j\pi u_2}{MN}(\hat{u}_2 \Delta ft(\hat{u}_2 \Delta ft - 1))} x_{SS}^{u_2}[0, 0]$$

$$\sum_{m=0}^{M-1} e^{-\frac{j\pi u_2}{MN}(mMN - \hat{u}_2 \Delta ft)(mMN - \hat{u}_2 \Delta ft + 1)}$$

$$= x_{SS}^{u_2*}[0, \hat{u}_2 \Delta ft] x_{SS}^{u_2}[0, 0] s_{SS}^{u_2}(0) \qquad (24)$$

Eqs. (23) and (24) indicate that the duality property of the ZC sequence is conserved between the delay-Doppler and time-frequency domains and between the time-frequency domain and time-domain, respectively. Further, (24) indicates that time-domain ZC can be obtained from delay-Doppler ZC by scaling it by constants $x_{SS}^{u_2}[0, 0]$ and $s_{SS}^{u_2}(0)$. In addition, the elements of the ZC sequence in the proposed SS are quantized before being mapped to DDRB (such as $\text{Re}\left\{x_{SS}^{u_2}[k, l]\right\} > 0 = 1$, $\text{Re}\left\{x_{SS}^{u_2}[k, l]\right\} < 0 = -1$, $\text{Im}\left\{x_{SS}^{u_2}[k, l]\right\} > 0 = j$, and $\text{Im}\left\{x_{SS}^{u_2}[k, l]\right\} < 0 = -j$) to
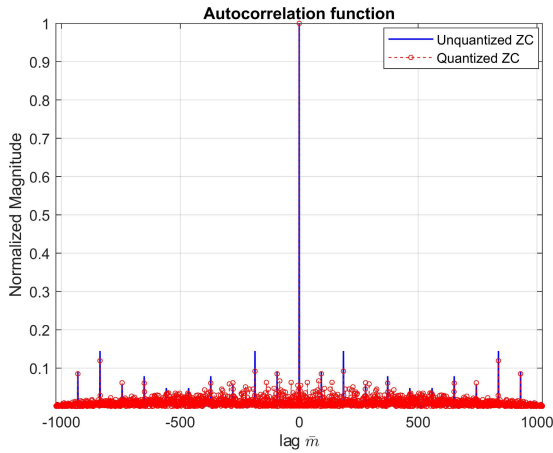
(a) Autocorrelation, $u_2 = 11$ and $u'_2 = 11$
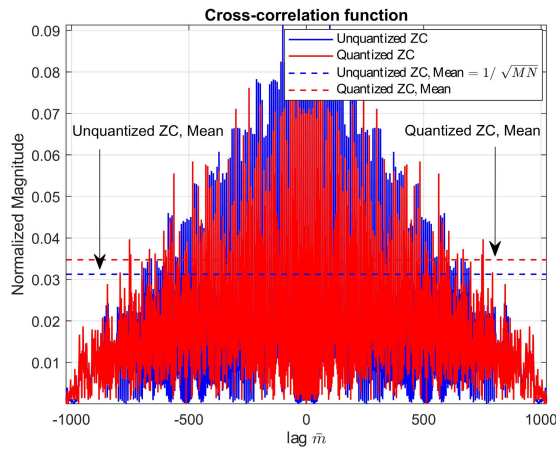
(b) Cross-correlation, $u_2 = 11$ and $u'_2 = 19$

FIGURE 8. Correlation property of the ZC sequence.

take advantage of the MP algorithm. Thus, $x_{SS}^{u_2}[k, l]$ takes the values from $\mathbb{A} \in \{1 + j, 1 - j, -1 + j, -1 - j\}$. In contrast to OFDM, where the Doppler spread in high-mobility environments induces ICI and degrades the performance, OTFS demonstrates no performance degradation because the efficient delay-Doppler channel fairly shifts the symbols from one DDRE to another without any loss of information [16], [22], [33].

Fig. 8 shows the correlation property of the ZC sequence as a function of lag $\bar{m}$. Figs. 8a and 8b show the autocorrelation function ($u_2 = 11$ and $u'_2 = 11$) and cross-correlation function ($u_2 = 11$ and $u'_2 = 19$), respectively, for both unquantized and quantized ZC sequences. As shown in Fig. 8a, the autocorrelation function of the ZC sequence preserves its characteristics and exhibits good autocorrelation when quantized to $\mathbb{A}$. As shown in Fig. 8b, the normalized mean value of cross-correlation function for unquantized ZC sequences is 0.0313 (i.e., $1/\sqrt{MN}$). The normalized mean value for quantized ZC sequences is 0.0347, which is slightly higher than that for quantized ZC sequences. Thus, the figures clearly show that the correlation properties of the ZC sequence hold even after the elements are quantized to $\mathbb{A}$.

Using (8) and (9), the SS received at the UE can be expressed as

$$r_{SS}(t) \triangleq \sum_{c=0}^{C-1} \sum_{i=1}^{P} \beta_i^c s_{SS}^c \left(t - \tau_i^c\right) e^{j2\pi v_i^c(t - \tau_i^c)} + w(t) \quad (25)$$

The signal $r_{SS}(t)$ in (25) sampled at $f_s = 1/T_s$ is given by

$$r_{SS}(\varsigma') = \sum_{c=0}^{C-1} \sum_{i=1}^{P} \beta_i^c s_{SS}^c \left(\varsigma' - \frac{\tau_i^c}{T_s}\right) e^{j2\pi v_i^c T_s \left(\varsigma' - \frac{\tau_i^c}{T_s}\right)} + w(\varsigma')$$

$$(26)$$

where $0 \leqslant \varsigma' < MN$. The n'^{th} OTFS symbol comprising M samples can be collected from (26) as follows:

$$r_{SS}\left(n'M + \ell\right)$$
$$= \sum_{c=0}^{C-1} \sum_{i=1}^{P} \beta_i^c s_{SS}^c \left(n'M + \ell - \frac{\tau_i^c}{T_s}\right) e^{j2\pi v_i^c T_s \left(n'M + \ell - \frac{\tau_i^c}{T_s}\right)}$$
$$+ w\left(n'M + \ell\right) \quad (27)$$

where $0 \leqslant n' < N$ and $0 \leqslant \ell < M$. Now, (27) is transformed into the time-frequency domain using discrete FT as

$$Y_{SS}[n', m']$$
$$= \frac{1}{M} \sum_{\ell=0}^{M-1} r_{SS}\left(n'M + \ell\right) e^{-j2\pi \frac{m'\ell}{M}}$$
$$= \frac{1}{M} \sum_{\ell=0}^{M-1} \sum_{c=0}^{C-1} \sum_{i=1}^{P} \beta_i^c s_{SS}^c \left(n'M + \ell - \frac{\tau_i^c}{T_s}\right)$$
$$e^{j2\pi v_i^c T_s \left(n'M - \frac{\tau_i^c}{T_s}\right)} e^{-j2\pi \frac{m'\ell}{M}}$$
$$+ \frac{1}{M} \sum_{\ell=0}^{M-1} w\left(n'M + \ell\right) e^{-j2\pi \frac{m'\ell}{M}}$$
$$= \sum_{c=0}^{C-1} \sum_{i=1}^{P} \beta_i^c e^{j2\pi v_i^c T_s \left(n'M - \frac{\tau_i^c}{T_s}\right)} e^{-j2\pi \frac{m'}{M} \frac{\tau_i^c}{T_s}} X_{SS}^c[n', m']$$
$$+ W[n', m'] \quad (28)$$

Using SFFT, (28) is transformed back to the delay-Doppler domain as

$$y_{SS}[k', l']$$
$$= \sum_{n'=0}^{N-1} \sum_{m'=0}^{M-1} Y_{SS}[n', m'] e^{j2\pi \left(\frac{m'l'}{M} - \frac{n'k'}{N}\right)}$$
$$= \sum_{n'=0}^{N-1} \sum_{m'=0}^{M-1} \sum_{c=0}^{C-1} \sum_{i=1}^{P} \beta_i^c e^{j2\pi v_i^c T_s \left(n'M - \frac{\tau_i^c}{T_s}\right)} e^{-j2\pi \frac{m'}{M} \frac{\tau_i^c}{T_s}}$$
$$X_{SS}^c[n', m'] e^{j2\pi \left(\frac{m'l'}{M} - \frac{n'k'}{N}\right)}$$
$$+ \sum_{n'=0}^{N-1} \sum_{m'=0}^{M-1} W[n', m'] e^{j2\pi \left(\frac{m'l'}{M} - \frac{n'k'}{N}\right)}$$
$$= \sum_{c=0}^{C-1} \sum_{i=1}^{P} \beta_i^c x_{SS}^c \left[\left(k' - k_i^c\right)_N, \left(l' - l_i^c\right)_M\right] + \hat{w}[k', l']$$

$$(29)$$

where $(\cdot)_M$ and $(\cdot)_N$ represent modulo M and N operations, respectively.

As seen in (29), the desired SS needs to be detected in the presence of intercell interference and noise because multiple SSs from adjacent BSs are received at the UE. Inspired by the MP algorithm in [34], a low-complexity algorithm is applied for SS detection. Let the OTFS symbol vector and channel matrix of the cth BS be denoted by $\mathbf{x}_{SS}^c \in \mathbb{C}^{MN \times 1}$ and $\mathbf{H}_{SS}^c \in \mathbb{C}^{MN \times MN}$, respectively. Here, it is assumed that the channel is correctly estimated using one of the algorithms in [21]–[27]. Then, (29) can be written as

$$\mathbf{y}_{SS} = \mathbf{H}_{SS}\mathbf{x}_{SS} + \mathbf{w} \tag{30}$$

where $\mathbf{y}_{SS} \in \mathbb{C}^{MN \times 1}$, $\mathbf{H}_{SS} = \left[\mathbf{H}_{SS}^0, \mathbf{H}_{SS}^1, \cdots, \mathbf{H}_{SS}^{C-1}\right]$, and $\mathbf{x}_{SS} = \left[(\mathbf{x}_{SS}^0)^T, (\mathbf{x}_{SS}^1)^T, \cdots, (\mathbf{x}_{SS}^{C-1})^T\right]^T$. Then, (30) can be modeled as a sparsely connected factor graph with MN variable and observation nodes corresponding to $\mathbf{x}_{SS}$ and $\mathbf{y}_{SS}$, respectively. Let the dth row of $\mathbf{H}_{SS}$, e^{th} column of $\mathbf{H}_{SS}$, variable node, and observation node be denoted by ψ_d, ψ_e, $x_{SS}(e)$, and $y_{SS}(d)$, respectively. In this factor graph, each $x_{SS}(e)$ is linked to the set of observation nodes $\{y_{SS}(\eta), \eta \in \psi_e\}$ and each $y_{SS}(d)$ is linked to the set of variable nodes $\{x_{SS}(\eta), \eta \in \psi_d\}$. For optimal detection of the transmitted SSs $\mathbf{x}_{SS}$, the joint maximum a posteriori (MAP) detection rule can be considered as follows:

$$\tilde{\mathbf{x}}_{SS} = \underset{\mathbf{x}_{SS} \in \mathbb{A}^{MN}}{\arg \max} \Pr\left(\mathbf{x}_{SS} \middle| \mathbf{y}_{SS}, \mathbf{H}_{SS}\right) \tag{31}$$

However, (31) incurs a large computational complexity and is difficult to be solved even for very small values of M and N. Hence, the symbols-in-succession MAP detection rule is considered for $0 \leqslant e < MN$ to detect the SS. With the initialization of the iteration, i.e., $q = 0$, the message passed from $y_{SS}(d)$ to $x_{SS}(e)$ is a Gaussian probability density function which can be computed as

$$y_{SS}(d) = x_{SS}(e) H_{SS}(d, e) + I_{de} \tag{32}$$

where $I_{de} = \sum_{\eta \in \psi_d} x_{SS}(\eta) H_{SS}(d, \eta) + w(d)$ represents the interference-plus-noise term approximated as a Gaussian random variable with mean and variance:

$$\mu_{de}^q = \mathbb{E}[I_{de}] = \sum_{\eta \in \psi_d, \eta \neq e} \sum_{g=1}^{|\mathbb{A}|} \Omega_{\eta d}^q [A(g)] A(g) H_{SS}(d, \eta) \tag{33}$$

$$(\sigma_{de}^q)^2 = \text{Var}(I_{de})$$
$$= \sum_{\eta \in \psi_d, \eta \neq e} \left(\begin{array}{c} \sum_{g=1}^{|\mathbb{A}|} \Omega_{\eta d}^q [A(g)] |A(g)|^2 |H_{SS}(d, \eta)|^2 \\ - \left| \sum_{g=1}^{|\mathbb{A}|} \Omega_{\eta d}^q [A(g)] A(g) H_{SS}(d, \eta) \right|^2 \end{array} \right)$$
$$+ \sigma^2 \tag{34}$$

where $\Omega[A(g)] | A(g) \in \mathbb{A}$ is the probability mass function (PMF) of symbols in $\mathbb{A}$ and σ is the noise variance. The message passed from $x_{SS}(e)$ to $y_{SS}(d)$ is the PMF

$$\Omega_{ed}^{q+1} = \xi \Omega_{ed}^q [A(g)] + (1 - \xi) \Omega_{ed}^{q-1} [A(g)]$$
$$\propto \prod_{\eta \in \psi_e, \eta \neq d} \Pr\left(y_{SS}(\eta) \middle| x_{SS}(e) = A(g), \mathbf{H}_{SS}\right) \tag{35}$$

where

$$\Pr\left(y_{SS}(\eta) \middle| x_{SS}(e) = A(g), \mathbf{H}_{SS}\right) \propto e^{-\frac{\left|y_{SS}(\eta) - \mu_{\eta e}^q - H_{SS}(\eta, e) A(g)\right|^2}{(\sigma_{\eta e}^q)^2}} \tag{36}$$

The convergence rate can be enhanced using the damping factor $\xi \in (0, 1]$ [37]. The messages keep passing from $y_{SS}(d)$ to $x_{SS}(e)$, and vice versa, until $\underset{e,d,A(j)}{\arg \max} \left| \Omega_{ed}^{q+1}[A(g)] - \Omega_{ed}^q[A(g)] \right| < \Xi$. Here, Ξ is a small number or $q = q_{max}$. Now, the decisions on the transmitted SSs are expressed as

$$\tilde{x}_{SS}(e) = \underset{A(g) \in \mathbb{A}}{\arg \max} \frac{1}{|\mathbb{A}|} \Pr\left(\mathbf{y}_{SS} \middle| x_{SS}(e) = A(g), \mathbf{H}_{SS}\right)$$
$$\approx \underset{A(g) \in \mathbb{A}}{\arg \max} \Omega_e [A(g)]$$
$$\approx \underset{A(g) \in \mathbb{A}}{\arg \max} \prod_{\eta \in \psi_e} \Pr\left(y_{SS}(\eta) \middle| x_{SS}(e) = A(g), \mathbf{H}_{SS}\right) \tag{37}$$

Then, the detected SSs in (37) are correlated with the reference SSs at the UE. The correlator's output for BS c is expressed as:

$$R_{SS}^c(\bar{m}) = \sum_{e=0}^{MN-1} \tilde{x}_{SS}(e) \left[x_{SS}^c(e + \bar{m})\right]^* \tag{38}$$

where $x_{SS}^c(e)$ is the 1D form of (22).

Finally, the desired SCID, u_2', is detected from the received SS by rearranging the elements of (38) into a 2D form with $0 \leqslant k' < N$ and $0 \leqslant l' < M$, such that $R_{SS}^c[k', l'] \in \mathbb{C}^{N \times M}$, as follows:

$$u_2' = \underset{u_2}{\arg \max} \left[\underset{k',l'}{\arg \max} \left|R_{SS}^c[k', l']\right|^2 > \gamma \right] \tag{39}$$

IV. SIMULATION

In this section, the performance of the proposed downlink synchronization technique for an OTFS-based cellular system in high-Doppler environments is evaluated and compared with that of an OFDM-based cellular system. A simple cellular model shown in Fig. 1 is used for the computer simulation, which assumes that the UE moves from BS0 to BS1. The carrier frequency (f_c) and Δf are set to 28 GHz and 15 kHz, respectively. For the channel, the 3GPP tapped delay line-C (TDL-C) model is used [38]. For the cth BS, the Doppler shift (v_i^c) is set to $v_{max} \cos(\theta_i^c)$ for the ith path, where $\theta_i^c \in [0, 2\pi)$ is an independent and uniformly distributed random

TABLE 1. OTFS Parameter set.

| Parameter	Value
Carrier Frequency, f_c	28 GHz
OTFS Symbol Size, $[N, M]$	[32,32]
UE Velocity, ν	{15, 75, 150} mph
Maximum Doppler Spread, v_{max}	{1.4, 7, 14} kHz
Channel Model	TDL-C
Subcarrier spacing, Δf	15 kHz
Doppler resolution, $1/NT$	468.75 Hz
Doppler resolution, $1/M\Delta f$	2.1 μs

variable [34]. The simulation parameters are summarized in Table 1.

Fig. 9 shows the detection probability of DP designed with cLFM and pLFM (with and without RP). The two BSs (BS0, BS1) transmit DPs with $N_{pLFM} = 1024$ and PCID $u_1 \in \{1, -1\}$. Here, it is assumed that the UE moves at $\nu \in \{15, 75, 150\}$ mph, which corresponds to $v_{max} \in \{1.4, 7, 14\}$ kHz at $f_c = 28$ GHz. Moreover, the UE is placed at the cell boundary of serving BS (BS0), implying that the signal-to-intercell interference ratio is 0 dB. In these figures, the detection probability of the DP transmitted from BS0 is shown. When both the ST and PCID detected at the UE are correct, the detection is considered "successful". Fig. 9a shows that, when the UE velocity is low, the detection probabilities are the same, i.e., 100% at an SNR of −12 dB, regardless of the waveform (cLFM and pLFM). However, the detection probability of cLFM degrades by 3 dB when $\nu = 75$ mph ($v_{max} = 7$ kHz) and falls to zero when $\nu = 150$ mph ($v_{max} = 14$ kHz), as shown in Figs. 9b and 9c. The detection probability of pLFM without RP degrades by 3 dB when $v_{max} = 7$ kHz and $\omega = 2$, degrades significantly when $v_{max} = 7$ kHz and $\omega = 10$, and converges to zero when $\nu = 150$ mph ($v_{max} = 14$ kHz). The detection probability of the pLFM with RP does not degrade for any ω when $v_{max} = 7$ kHz, degrades by 3 dB when $v_{max} = 14$ kHz and $\omega = 2$, and does not degrade when $v_{max} = 14$ kHz and $\omega = 10$. These results can be expected from Fig. 6b because, for the cases of cLFM and pLFM without RP, a time shift occurs in the presence of Doppler shift. In these cases, the detection probability decreases in proportion to the UE velocity. However, the performance degradation is significantly reduced in the case of pLFM with RP because an accurate ST can be obtained in high-Doppler environments, as shown in Fig. 6b. Note that the detection probability obtained by the pLFM with RP ($\omega = 10$) in a high-mobility environment ($\nu = 150$ mph) is similar to that obtained in a low-mobility environment ($\nu = 15$ mph). Therefore, the effect of Doppler shift on ST and PCID detection can be significantly reduced using the proposed DP (pLFM with RP).
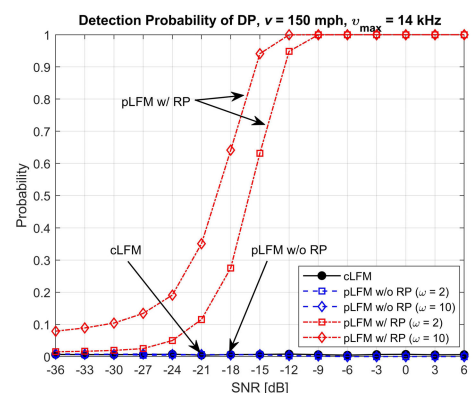
Fig. 10 shows the detection probability of the SS designed with two OTFS symbols (pilot DDRB and SS DDRB). Here, the delay-Doppler channel is assumed to be correctly estimated using the pilots discussed in Section III-B, and the SSs are generated at BS0 and BS1 with $u_2 = 11$ and $u_2 = 19$, respectively. Here, the detection is declared
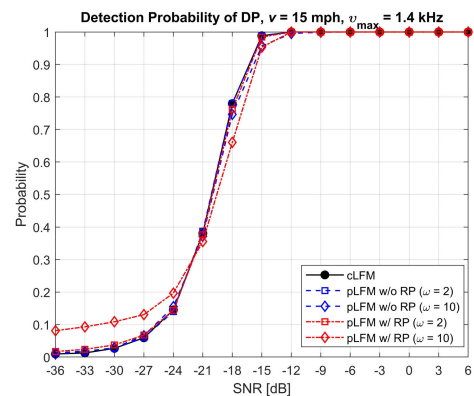

(a) $v_{max} = 1.4$ kHz
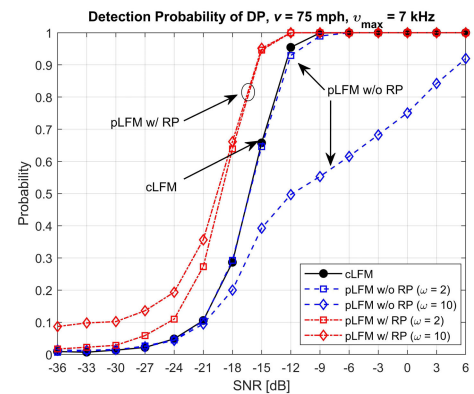

(b) $v_{max} = 7$ kHz

(c) $v_{max} = 14$ kHz

FIGURE 9. Detection probability of DP under high-mobility two-cell multipath environment.

"successful" when the SCID detected at the UE is correct. Fig. 10 shows that, for all three Doppler frequencies, the detection probability reaches 100% at an SNR of −21 dB using the proposed technique (OTFS). In addition, in the figure, the detection probability is compared with the results obtained by the conventional technique (OFDM). In conventional techniques, the ZC sequence is mapped to an OFDM symbol. For a fair comparison, the parameters such as ZC sequence length, Δf, and f_c are maintained constant. The figure (OFDM) shows that when the Doppler frequency is
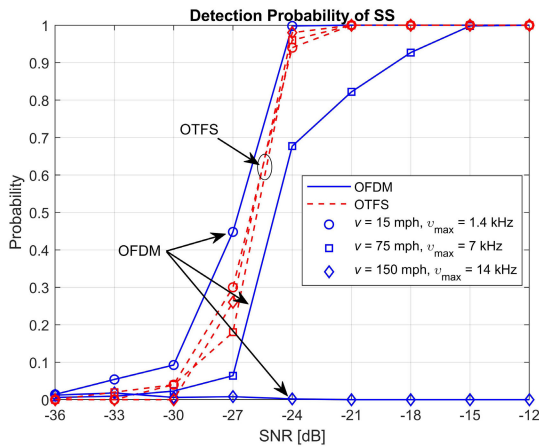
FIGURE 10. Detection Probability of SS using the OFDM and proposed OTFS techniques.
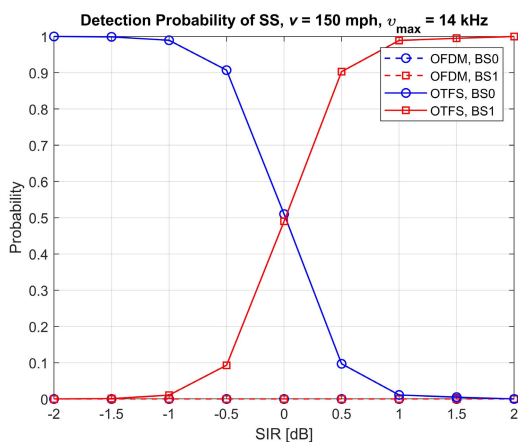
FIGURE 11. Detection Probability of SS in a high-mobility two-cell environment.

low (i.e., $v_{max} = 1.4$ kHz), a 100% detection probability can be obtained at an SNR of -21 dB. However, as the Doppler frequency increases, the time-domain ZC sequence will be distorted and time-shifted, resulting a decrease in detection probability. This time shift causes a cyclic shift in the frequency-domain and results in zero correlation between the desired and cyclic-shifted ZC sequences. Therefore, when $v_{max} = 7$ kHz, the detection probability degrades by 6 dB as compared to $v_{max} = 1.4$ kHz and falls to zero at all SNR regions when $v_{max} = 14$ kHz. These results indicate that the SS designed with the proposed technique (OTFS) is robust in high-Doppler environments, whereas the detection probability of the OFDM case is reduced to zero in all SNR regions when $v_{max} > \Delta f / 2$.

Fig. 11 shows the detection probability of SS when the UE moves from BS0 to BS1 at $v = 150$ mph. It can be seen from this figure that as the signal-to-interference ratio (SIR) increases, the cell detection probability of the target BS (i.e., BS1) increases. Here, SIR represents the ratio of the signal power from the target BS to that from the serving BS (i.e., BS0). From this figure, it can be concluded that the target

BS can be correctly detected using the proposed technique (OTFS). However, the detection probability becomes zero over all SIR regions when OFDM is used in high-Doppler environments ($v_{max} = 14$ kHz).

V. CONCLUSION

This paper proposes a downlink synchronization and CID estimation technique for OTFS-based cellular systems in high-Doppler environments. To provide accurate ST estimation and a large number of CIDs in high-Doppler environments, a frame structure for downlink synchronization is proposed, which comprises a DP, a pilot, and an SS. The DP is designed using the pLFM because it can provide accurate ST and PCID in high-Doppler environments without any prior information (channel, ST). The autocorrelation and cross-correlation functions of pLFM are examined to investigate their correlation properties when subjected to a high Doppler shift. To reduce the undesirable properties of the autocorrelation function (side peak and time ambiguity), an RP scheme is developed for pLFM. After completing the ST synchronization with DP, the pilot transmitted in the delay-Doppler domain is used to estimate the delay-Doppler channel. The SS is designed with a ZC sequence and detected coherently in the delay-Doppler domain. After deriving the duality property of the ZC sequence, it is shown that the properties of the ZC sequence are conserved when transformed from the delay-Doppler domain to the time-frequency domain and time-frequency domain to time-domain. Finally, a low-complexity MP-based detection algorithm is applied to detect the SCID at the UE. The simulation results confirm that the pLFM with RP is suitable for DP design because it can provide an accurate ST in the presence of a high Doppler shift. The cross-correlation level of pLFM is small, which implies that the intercell interference is not significant. The ZC-based SS is suitable for OTFS-based cellular systems because it can provide a large number of CIDs in high-Doppler environments and produce a small intercell interference (cross-correlation function). Moreover, the detection probability decreases significantly in high-mobility scenarios when OFDM is used. The proposed downlink synchronization technique can be successfully used for OTFS-based cellular systems because the detection probabilities of DP and SS do not degrade in high-Doppler environments.

REFERENCES

[1] *Technical Specification Group Radio Access Network; 5G; Study on Scenarios and Requirements for Next Generation Access Technologies (Release 16)*, document 3GPP 38.913, Rev. 16.0.0, Jul. 2020.

[2] M. Muhammad and G. A. Safdar, "Survey on existing authentication issues for cellular-assisted V2X communication," *Veh. Commun.*, vol. 12, pp. 50–65, Apr. 2018.

[3] *LTE, Evolved Universal Terrestrial Radio Access (E-UTRA); Base Station (BS) Radio Transmission and Reception*, Standard 38.104, Rev. 8.6.0, Jul. 2009.

[4] Y. S. Cho, J. Kim, W. Y. Yang, and C. G. Kang, *MIMO-OFDM Wireless Communications With MATLAB*. Hoboken, NJ, USA: Wiley, Aug. 2010.

[5] S. Das and P. Schniter, "Max-SINR ISI/ICI-shaping multicarrier communication over the doubly dispersive channel," *IEEE Trans. Signal Process.*, vol. 55, no. 12, pp. 5782–5795, Dec. 2007.

[6] K. Fang, L. Rugini, and G. Leus, "Low-complexity block turbo equalization for OFDM systems in time-varying channels," *IEEE Trans. Signal Process.*, vol. 56, no. 11, pp. 5555–5795, Aug. 2008.

[7] K. Liu, T. Kadous, and A. M. Sayeed, "Orthogonal time-frequency signaling over doubly dispersive channels," *IEEE Trans. Inf. Theory*, vol. 50, no. 11, pp. 2583–2603, Nov. 2004.

[8] Y. Zhao and S.-G. Haggman, "Intercarrier interference self-cancellation scheme for OFDM mobile communication systems," *IEEE Trans. Commun.*, vol. 49, no. 7, pp. 1185–1191, Jul. 2001.

[9] G. Leus, S. Zhou, and G. B. Giannakis, "Orthogonal multiple access over time- and frequency-selective channels," *IEEE Trans. Inf. Theory*, vol. 49, no. 8, pp. 1942–1950, Aug. 2003.

[10] *Technical Specification Group Radio Access Network; NR; Phys. Channels Modulation (Release 15)*, Standard 38.211, Rev. 15.2.0, Jun. 2018.

[11] M. Asim, R. Pec, T. H. Im, and Y. S. Cho, "Cell search techniques for underwater acoustic cellular systems," *IEEE Access*, vol. 7, pp. 106019–106033, Aug. 2019.

[12] M. S. Khan, R. Pec, C. H. Park, and Y. S. Cho, "Random access preamble design for high-velocity user in millimeter-wave cellular networks," *IEEE Access*, vol. 6, pp. 66047–66054, Nov. 2018.

[13] M. S. Khan, C. H. Park, J. Joung, and Y. S. Cho, "Doppler-tolerant sequence design for positioning high-speed vehicles in millimeter-wave cellular systems," *Veh. Commun.*, vol. 30, Aug. 2021, Art. no. 100358.

[14] Z. Wang, S. Zhou, G. B. Giannakis, C. R. Berger, and J. Huang, "Frequency-domain oversampling for zero-padded OFDM in underwater acoustic communications," *IEEE J. Ocean. Eng.*, vol. 37, no. 1, pp. 14–24, Jan. 2012.

[15] X.-G. Xia, "Precoded and vector OFDM robust to channel spectral nulls and with reduced cyclic prefix length in single transmit antenna systems," *IEEE Trans. Commun.*, vol. 49, no. 8, pp. 1363–1374, Aug. 2001.

[16] R. Hadani, S. Rakib, M. Tsatsanis, and A. Monk, "Orthogonal time frequency space modulation," in *Proc. IEEE Wireless Commun. Netw. Conf. (WCNC)*, San Francisco, CA, USA, Mar. 2017, pp. 1–6.

[17] G. D. Surabhi, R. M. Augustine, and A. Chockalingam, "Peak-to-average power ratio of OTFS modulation," *IEEE Commun. Lett.*, vol. 23, no. 6, pp. 999–1002, Jun. 2019.

[18] V. Khammammetti and S. K. Mohammed, "OTFS-based multiple-access in high Doppler and delay spread wireless channels," *IEEE Wireless Commun. Lett.*, vol. 8, no. 2, pp. 528–531, Apr. 2019.

[19] A. K. Sinha, S. K. Mohammed, P. Raviteja, Y. Hong, and E. Viterbo, "OTFS based random access preamble transmission for high mobility scenarios," *IEEE Trans. Veh. Technol.*, vol. 69, no. 12, pp. 15078–15094, Dec. 2020.

[20] Z. Ding, R. Schober, P. Fan, and H. Vincent Poor, "OTFS-NOMA: An efficient approach for exploiting heterogenous user mobility profiles," *IEEE Trans. Commun.*, vol. 67, no. 11, pp. 7950–7965, Nov. 2019.

[21] P. Raviteja, K. T. Phan, and Y. Hong, "Embedded pilot-aided channel estimation for OTFS in delay–Doppler channels," *IEEE Trans. Veh. Technol.*, vol. 68, no. 5, pp. 4906–4917, May 2019.

[22] K. R. Murali and A. Chockalingam, "On OTFS modulation for high-Doppler fading channels," in *Proc. Inf. Theory Appl. Workshop (ITA)*, San Diego, CA, USA, Feb. 2018, pp. 1–10.

[23] A. Fish, S. Gurevich, R. Hadani, A. M. Sayeed, and O. Schwartz, "Delay-Doppler channel estimation in almost linear complexity," *IEEE Trans. Inf. Theory*, vol. 59, no. 11, pp. 7632–7644, Nov. 2013.

[24] M. Kollengode Ramachandran and A. Chockalingam, "MIMO-OTFS in high-Doppler fading channels: Signal detection and channel estimation," in *Proc. IEEE Global Commun. Conf. (GLOBECOM)*, Abu Dhabi, UAE, Dec. 2018, pp. 206–212.

[25] R. Hadani and S. S. Rakib, "OTFS methods of data channel characterization and uses thereof," U.S. Patent 9 444 514 B2, Sep. 13, 2016.

[26] Y. Liu, S. Zhang, F. Gao, J. Ma, and X. Wang, "Uplink-aided high mobility downlink channel estimation over massive MIMO-OTFS system," *IEEE J. Sel. Areas Commun.*, vol. 38, no. 9, pp. 1994–2009, Sep. 2020.

[27] W. Shen, L. Dai, J. An, P. Fan, and R. W. Heath, "Channel estimation for orthogonal time frequency space (OTFS) massive MIMO," *IEEE Trans. Signal Process.*, vol. 67, no. 16, pp. 4204–4217, Aug. 2019.

[28] C. Jin, Z. Bie, X. Lin, W. Xu, and H. Gao, "A simple two-stage equalizer for OTFS with rectangular windows," *IEEE Commun. Lett.*, vol. 25, no. 4, pp. 1158–1162, Apr. 2021, doi: 10.1109/LCOMM.2020.3043841.

[29] R. Nee and R. Prasad, *OFDM for Wireless Multimedia Communications*. Norwood, MA, USA: Artech House, 2000.

[30] F. Hlawatsch and G. Matz, *Wireless Communications Over Rapidly Time-Varying Channels*. New York, NY, USA: Academic, 2011.

[31] F. Khan, *LTE for 4G Mobile Broadband: Air Interface Technologies and Performance*. Cambridge, U.K.: Cambridge Univ. Press, 2009.

[32] X. Liu and D. Qiao, "Location-fair beamforming for high speed railway communication systems," *IEEE Access*, vol. 6, pp. 28632–28642, May 2018.

[33] P. Raviteja, K. T. Phan, Y. Hong, and E. Viterbo, "Interference cancellation and iterative detection for orthogonal time frequency space modulation," *IEEE Trans. Wireless Commun.*, vol. 17, no. 10, pp. 6501–6515, Oct. 2018.

[34] P. Raviteja, K. T. Phan, Q. Jin, Y. Hong, and E. Viterbo, "Low-complexity iterative detection for orthogonal time frequency space modulation," in *Proc. IEEE Wireless Commun. Netw. Conf. (WCNC)*, Barcelona, Spain, Apr. 2018, pp. 1–6.

[35] B. R. Mahafza, *Radar Systems Analysis and Design Using MATLAB*. Boca Raton, FL, USA: CRC Press, 2013.

[36] Z. G. Liu, "Residue theorem and theta function identities," *Ramanujan J.*, vol. 5, pp. 129–151, Jun. 2001.

[37] M. Pretti, "A message-passing algorithm with damping," *J. Stat. Mech.: Theory Exp.*, vol. 2005, no. 11, Nov. 2005, Art. no. P11008.

[38] *Technical Specification Group Radio Access Network; Study Channel Model for Frequencies From 0.5 to 100 GHz (Release 16)*, document 3GPP 38.901, Rev. 16.1.0, Dec. 2019.

MOHAMMED SAQUIB KHAN (Student Member, IEEE) was born in Mumbai, Maharashtra, India, in 1994. He received the B.E. degree in electronics and telecommunication engineering from Mumbai University, Mumbai, in 2015, and the Ph.D. degree in electrical and electronics engineering from Chung-Ang University, Seoul, South Korea, in 2020.

During his Ph.D., he worked as a Research Assistant with the Mobile Communications Laboratory, Chung-Ang University, Seoul, where he is currently engaged in Postdoctoral Research. His research interests include wireless communication systems, digital signal processing, and machine learning.

Dr. Khan is a member of the Korea Institute of Communications and Information Sciences. He received the Chung-Ang University Young Scientist Scholarship (CAYSS) for his M.S. and Ph.D. degrees and the Samsung Humantech Paper Encouragement Award, in 2020.

YEONG JUN KIM was born in South Korea, in 1981. He received the B.S., M.S., and Ph.D. degrees in electrical and electronics engineering from Chung-Ang University, Seoul, South Korea, in 2005, 2007, and 2011, respectively.

From 2005 to 2011, he was a Research Assistant with the Mobile Communications Laboratory, Chung-Ang University. From 2011 to 2015, he worked at LIG NEX1, South Korea, as a Senior Research Engineer. He was involved in developing modems for multiband and multirole radio. Since 2015, he has been working as the Deputy Principal Research Engineer with LG Electronics Company, Seoul. He has been involved in standardization of 5G NR and development of MODEM chipset for LTE-A and 5G. He is the author of more than 50 conference and articles. His research interests include the area of mobile communication and digital signal processing, especially for MIMO-OFDM and 5G.

QASIM SULTAN was born in Pakistan, in 1994. He received the B.S. degree in electrical and telecommunications engineering from COMSATS University, Islamabad, Pakistan, in 2017, and the M.S. degree in electrical and electronics engineering from Chung-Ang University, Seoul, South Korea, in 2019, where he is currently pursuing the Ph.D. degree in electrical and electronics engineering.

Since 2017, he has been working as a Research Assistant with the Mobile Communications Laboratory, Chung-Ang University. His research interests include areas of wireless communication systems and digital signal processing. He was a recipient of Chung-Ang University Young Scientist Scholarship (CAYSS).

JINGON JOUNG (Senior Member, IEEE) received the B.S. degree in radio communication engineering from Yonsei University, Seoul, South Korea, in 2001, and the M.S. and Ph.D. degrees in electrical engineering and computer science from KAIST, Daejeon, South Korea, in 2003 and 2007, respectively.

He was a Postdoctoral Fellow with KAIST, South Korea and UCLA, CA, USA, in 2007 and 2008, respectively. From 2009 to 2015, he was a Scientist with the Institute for Infocomm Research (I^2R), Agency for Science, Technology and Research (A*STAR) Singapore. In 2016, he joined Chung-Ang University (CAU), Seoul, as a faculty member. He is currently an Associate Professor with the School of Electrical and Electronics Engineering, CAU, where he is also the Principal Investigator with the Intelligent Wireless Systems Laboratory. His research interests include communication signal processing, numerical analysis, algorithms, and machine learning.

Dr. Joung was a recipient of the First Prize of the Intel-ITRC Student Paper Contest, in 2006. He was recognized as the Exemplary Reviewers of the IEEE COMMUNICATIONS LETTERS, in 2012 and the IEEE WIRELESS COMMUNICATIONS LETTERS, in 2012, 2013, 2014, and 2019. He served as the Guest Editor for the IEEE ACCESS, in 2016. He served on the Editorial Board of the APSIPA Transactions on Signal and Information Processing, from 2014 to 2019, and served as a Guest Editor for the *Electronics* (MDPI), in 2019. He is currently serving as an Associate Editor for the IEEE TRANSACTIONS ON VEHICULAR TECHNOLOGY and *Sensors* (MDPI).

YONG SOO CHO (Senior Member, IEEE) was born in South Korea. He received the B.S. degree in electronics engineering from Chung-Ang University, Seoul, South Korea, in 1984, the M.S. degree in electronics engineering from Yonsei University, Seoul, in 1987, and the Ph.D. degree in electrical and computer engineering from The University of Texas, Austin, TX, USA, in 1991.

In 1984, he was a Research Engineer with Goldstar Electrical Company, Osan, South Korea. In 2001, he was a Visiting Research Fellow with the Electronics and Telecommunications Research Institute. Since 1992, he has been a Professor with the School of Electrical and Electronics Engineering, Chung-Ang University, Seoul. He is the author of 12 books, more than 400 conference and articles, and more than 120 patents. His research interests include the area of mobile communication and digital signal processing, especially for MIMO OFDM and 5G.

Dr. Cho served as the President of the Korean Institute of Communications and Information Sciences, in 2016. He was a recipient of Dr. Irwin Jacobs Award, in 2013.

. . .